AGU PUBLICATIONS

Geophysical Research Letters

RESEARCH LETTER
10.1002/2014GL061994

Key Points:
- O_3 residual flux by BDC does not sync with cross-tropopause O_3 fluxes
- More accurate diagnostics of ozone STE are needed in climate-chemistry models
- TC and LS methods are suitable for diagnosing STE of ozone

Supporting Information:
- Readme
- Figure S1
- Figure S2

Correspondence to:
J. Hsu,
juno.hsu@uci.edu

Citation:
Hsu, J., and M. J. Prather (2014), Is the residual vertical velocity a good proxy for stratosphere-troposphere exchange of ozone?, *Geophys. Res. Lett.*, *41*, 9024–9032, doi:10.1002/2014GL061994.

Received 24 SEP 2014
Accepted 13 NOV 2014
Accepted article online 20 NOV 2014
Published online 16 DEC 2014

Is the residual vertical velocity a good proxy for stratosphere-troposphere exchange of ozone?

Juno Hsu[1] and Michael J. Prather[1]

[1] Department of Earth System Science, University of California, Irvine, California, USA

Abstract Stratosphere-troposphere exchange (STE) of ozone (O_3) is key in the budget of tropospheric O_3, in turn affecting climate forcing and global air quality. We compare three commonly used diagnostics meant to quantify cross-tropopause O_3 fluxes with a Chemistry-Transport Model driven by two distinct European Centre forecast fields. Our reference case calculates accurate, geographically resolved net transport across an isosurface in artificial tracer e90 representing the tropopause. Hemispheric fluxes derived from the ozone mass budget of the lowermost stratosphere yield similar results. Use of the Brewer-Dobson residual vertical velocity as a scaled proxy for ozone flux, however, fails to capture the interannual variability. Thus, the common notion that the strength of stratospheric overturning circulation is a good measure for global STE does not apply to O_3. Climatic variability in the modeled O_3 flux needs to be diagnosed directly rather than indirectly through the overturning circulation.

1. Introduction

The primary oxidant of the troposphere is O_3. Its reaction with H_2O generates hydroxyl radicals (OH) that destroy pollutants and clean the lower atmosphere [*Logan et al.*, 1981; *Thompson*, 1992]. Increases in tropospheric O_3 over the industrial era make it the third most important greenhouse gas after CO_2 and CH_4 [*Myhre et al.*, 2013], and this increase also poses threats to air quality globally [*Fiore et al.*, 2012]. The global burden of tropospheric O_3 (~ 340 Tg) is maintained by a balance between photochemical tropospheric production (~ 5100 Tg/yr) and loss (~ 4650 Tg/yr), surface losses (~ 1000 Tg/yr), and influx from the stratosphere (~ 550 Tg/yr) as estimated from multimodel studies [*Stevenson et al.*, 2006; *Young et al.*, 2013]. Unfortunately in these studies, the net stratospheric influx is a small residual with a large uncertainty range as a result of balancing the three large terms that are inconsistently calculated among climate-chemistry models (CCMs; see Table 2 in *Young et al.* [2013]). The inferred STE calculated from the tropospheric ozone photochemistry budget is also found to be sensitive to the choice for the upper boundary of the troposphere (see Table 2 in *Stevenson et al.* [2004]). For a summary of the mean O_3 STE of from all recent studies including estimates from observations, see Table 8.1 of the fifth Intergovernmental Panel on Climate Change assessment report [*Myhre et al.*, 2013].

Several other STE diagnostics have been developed and used in parallel by the community. An evaluation of these diagnostics using the same meteorological data and models has never been presented. Here we implement three commonly used STE diagnostic methods in the 3-D University of California Irvine Chemistry-Transport Model (CTM) driven by European Centre for Medium-Range Weather Forecasts (ECMWF) Integrated Forecast System (IFS) data. These methods include the following: (1) The tropospheric column method (TC method hereafter [*Hsu et al.*, 2005]), applied without invoking photochemistry in the troposphere, tracks the net change in O_3 on the tropospheric side of a tropopause-like isosurface for each tropospheric grid column; (2) The lowermost stratosphere method (LS method hereafter) infers the net hemispheric fluxes across the extratropical tropopause by calculating all other terms of the O_3 budget within the lowermost stratosphere (LMS, from the tropopause isosurface to a standard upper level such as 100 hPa or 380 K to separate it from the middle world). The LS method is first devised by *Appenzeller et al.* [1996] to derive STE fluxes of air mass. (3) Our Brewer-Dobson method (BD method hereafter [*Holton*, 1990]) calculates the monthly mean vertical residual velocity ($\overline{w}^*$) from the transformed Eulerian mean equations [*Andrews et al.*, 1987] and combines with the coincident average ozone ($\overline{O_3}$) to calculate a flux ($\overline{w}^* \overline{O_3}$). The residual circulation approximates the zonal mean Lagrangian circulation induced by small-amplitude waves (here the zonal mean is denoted with an overbar, and the residual velocity by an asterisk). The method of *Wei* [1987] is not considered here because it involves the interpolation of gridded meteorological data onto

the defined tropopause, and this extra step can introduce major errors into the STE estimates [*Gettelman and Sobel*, 2000].

This paper examines the consistency of the magnitude, location, and interannual variability of O_3 STE as calculated using these three methods. For TC diagnostics, the accuracy of O_3 fluxes across a defined 3-D tropopause-like surface (see section 2.2) is subject only to the model's finite temporal and spatial resolutions (see *Prather et al.* [2008] for advection errors due to finite resolution). Likewise, for the LS method, the integrated hemispheric fluxes can be accurately calculated. Small differences can be attributed to the upward O_3 fluxes at the tropical tropopause, which are not enclosed by the LMS domain. The LMS mass tendency term (the so-called "breathing" of the LMS; also noted as dM/dt_{LMS} later) is important for the seasonal cycle of STE of air mass or O_3 [*Appenzeller et al.*, 1996; *Tie and Hess*, 1997; *Olsen et al.*, 2004] while its importance for interannual variability of STE is not known. For example, the mass tendency was not considered in the study of *Olsen et al.* [2013] because of the poor vertical coverage in Aura Microwave Limb Sounder satellite O_3 data in the LMS. Ozone chemistry in the LMS is often neglected [*Olsen et al.*, 2004, 2013] on the basis of being slow compared to transport (on the order of 1/1000 days^{-1}; Figure 2 of *McLinden et al.* [2000]); however, its contribution to the STE of ozone has never been formally quantified.

The BD method is based on the theoretical idea that the downward mass transport by the overturning Brewer-Dobson circulation (BDC) is a useful measure for the global-scale STE on seasonal or longer time series [*Holton et al.*, 1995] and thus has been used as a scaled proxy for ozone flux because ozone abundances are much larger in the stratosphere [*Gettelman et al.*, 1997]. If it is a good measure, one can calculate this term in conjunction with the breathing of the LMS to relate to the cross-tropopause fluxes as in *Hegglin and Shepherd* [2009]. Validation of the BD method is examined here because this approach not only assumes that eddy transports (from horizontal or vertical zonal asymmetry) are negligible for bringing ozone to the LMS but also implies that if it works, the long-term variation of the stratospheric wave drag that drives the BDC can be a good indicator for STE of ozone. Indeed, the finding that the residual circulation under increases of Greenhouse gases is strengthened [*Butchart et al.*, 2010] provides the basis for inferring without explicit calculations that STE of ozone increases under climate change in recent Climate Model Intercomparison Project Phase 5 (CMIP5) [*Eyring et al.*, 2013]. Here we are able to diagnose accurate STE of O_3 based on the TC and LS methods to verify if the BD approximation is valid.

Here O_3 STE is diagnosed in two separate simulations driven by two different cycles (29r1 versus 36r1) of ECMWF-IFS data over similar time periods (see section 2.1). For each simulation, the O_3 STE calculated by the TC method uses the tropopause defined by the synthetic tracer e90 [*Prather et al.*, 2011] and serves as the reference (as TC-e90 flux) for comparison against all other diagnosed STE fluxes. In section 3.1, we examine the pathway by which O_3 enters the LMS and crosses several tropopause-like surfaces. We find that ozone enters the LMS from middle to high latitudes predominantly during the winter season. The transport then turns more horizontal and equatorward and crosses the tropopause surfaces at midlatitudes/subtropics during the spring. In terms of the hemispherically integrated STE fluxes, similar values are obtained across all chosen isosurfaces with the TC and LS methods. In terms of seasonality, the Northern Hemisphere (NH) (not Southern Hemisphere (SH)) residual fluxes from the BD method do capture the phase of the seasonal cycle but with a magnitude that is about twice as large. Section 3.2 examines interannual variability. For each simulation, fluxes from TC or LS methods are highly correlated. Further up in altitude at 100 hPa, the exact simulated flux correlates best with the TC-e90 flux with a 3 month time lead. However, the residual O_3 flux from the BD method, with a much larger variability, fails to match any calculated interannual variation of STE, even when the time lead is varied. Across the two simulations, the interannual variations of STE are very different from each other. In contrast, the residual fluxes advected by the large-scale BDC across 100 hPa remain similar.

Section 4 summarizes our results, including the obvious recommendation that more accurate methods for diagnosing STE O_3 fluxes be adopted in CCMs. We demonstrate that the BD method relying solely on the residual vertical velocity fails to characterize the magnitude and also climate variability of the flux. As illustrated here with two distinct meteorologies, we find O_3 STE is sensitive to quasi-horizontal mixing processes and the long term variation of the LMS mass.

2. Method

2.1. Model Setup and Meteorological Data

In the UCI CTM, the stratospheric O_3 chemistry (net $P - L$) is simulated using the linearized O_3 scheme, Linoz v3.0 with prognostic O_3-N_2O-NO_y-CH_4 chemistry [*Hsu and Prather*, 2010] and with surface abundances of long-live tracers fixed at year 2000 level. We also include two tracers: e90 to define the tropopause [*Prather et al.*, 2011] and age-of-air as the mean age of an air mass since entering the stratosphere [*Waugh and Hall*, 2002]. Two sets of T42L60 ECMWF-IFS data are used: 3 h averaged meteorological data at ~ 2.8° horizontal resolution and ~ 1 km vertical resolution in the lower stratosphere; IFS Cycle 29r1 (C29 hereafter) data for years 2000–2006 and IFS Cycle 36r1 (C36 hereafter) for years 2000–2007. Each simulation is first spun up for 10 years by recycling year 2000 meteorology. Changes in parameterization and assimilation processes made for each cycle of ECMWF-IFS can be found at http://www.ecmwf.int/en/forecasts/documentation-and-support/changes-ecmwf-model.

Differences between the two cycles in large-scale transport and O_3 photochemistry of the lower stratosphere are summarized in Figures S1 and S2 in the supporting information. Transport diagnostics are taken from *Strahan et al.* [2011]. Relative to C29, the C36 simulation has a slower ascent and a more sluggish overturning circulation as evidenced by the older tropical mean age-of-air and the larger horizontal gradient of age between the midlatitude and the tropics (see Figures S1a and S1b). More vigorous lateral mixing in C36 between surf zone and tropical pipe is concluded from the smaller tropical N_2O abundances (Figure S1c) despite there being overall less tropical photochemical loss. The N_2O and mean age correlation for C29 is closer to the observed range (shaded green in Figure S1d) [*Strahan et al.*, 2011]. The net production of O_3 below 100 hPa and above the tropopause is 57 Tg/yr for C36, and much less, 15 Tg/yr, for the vigorous circulation of C29.

2.2. Diagnostics of Cross-Isosurface O_3 Fluxes

A state variable for each air mass is needed to map out 3-D surfaces separating the stratosphere from the troposphere for each grid cell in the CTM. Here we define these 3-D isosurfaces by chemical tracers, either the artificial tracer e90 or O_3 itself. The e90 tracer is emitted uniformly from the surface and destroyed uniformly with a loss frequency of 1/(90 days) throughout the atmosphere. Emissions are scaled to achieve a global mean value of 100 ppb, and the tropopause defined by the temperature lapse rate is accurately described by the 90 ppb e90-surface (see details in *Prather et al.* [2011]). Ozone isosurfaces have also been used to mark the tropopause, but as shown in *Considine et al.* [2008] the value of O_3 at the northern midlatitude tropopause varies seasonally by 50 ppb or more. To test the sensitivity to the tropopause location, we also calculate STE O_3 fluxes across O_3 isosurfaces of 120 ppb and 250 ppb.

The second-order moments advection scheme [*Prather*, 1986] calculates tracer fluxes across the six surfaces of each CTM grid box. Fluxes are accumulated when they cross a grid box surface that lies on the isosurface. Thus, we compute O_3 fluxes directly into and out of the LMS for each time step, defining the LMS bounded above by the 100 hPa isobaric surface and below by the e90-tropopause (LS-e90), the 120 ppb-O_3 surface (LS-120 ppb), or the 250 ppb-O_3 surface (LS-250 ppb). If the top and bottom surfaces do not cross in the tropics, then the equator is used to separate the two hemispheres. The hemispheric LS O_3 STE is calculated monthly as the residual of balancing (i) the net O_3 influx across the 100 hPa surface from the pole to the tropical boundary of the LMS, (ii) the net photochemical source within the LMS region, and (iii) the change in the daily averaged LMS O_3 mass through the month, e.g., LS-e90= $wO_{3\mathrm{LMS@100hPa}} + (P-L)_{\mathrm{LMS}} - \mathrm{d}M/\mathrm{d}t_{\mathrm{LMS}}$.

For TC the O_3 STE is calculated based on the change in tropospheric O_3 content after each tracer transport step using an isosurface (e90, 120 ppb-O_3, 250 ppb-O_3) to mark the tropopause. This method is developed by *Hsu et al.* [2005] and further improved by *Hsu and Prather* [2009] to produce less noisy geographic maps of STE flux. Three TC STE fluxes are named as TC-e90, TC-120 ppb, and TC-250 ppb. The monthly, zonal-mean vertical residual velocity ($\overline{w^*}$) at 100 hPa is calculated based on the equation (3.5.1b) of *Andrews et al.* [1987]. The residual O_3 flux is written as $\overline{w^*}\,\overline{O_3}$. We also accumulate the exact simulated vertical flux across 100 hPa surface for each time step, denoted as $\overline{wO_{3\mathrm{NH}}}$ with the subscript of "LMS" or "NH" indicating the area of integration.

3. Results

3.1. Seasonality

Figures 1a–1c shows the zonally averaged meridional and vertical O_3 transport for the January, April, and July monthly means over the 7 year period from the C29 simulation. The magnitude of the O_3 transport (color contours; in ppb/d) is obtained by integrating the ozone flux (moles-O_3/s/m^2) across the surface of the model grid box that is normal to the flux and is then normalized by the air mass of the grid box (moles-air). The transport everywhere is adjusted to the value with respect to a grid box with a uniform latitudinal length of 300 km and a vertical depth of 1.5 km in geometric height for fair comparison (see supporting information text for more discussion). The direction of the O_3 transport is shown in arrows of unit length. The positions of the different isosurfaces are approximated from the monthly zonal mean values: e90 tropopause (black); 120 ppb and 250 ppb O_3 surfaces (dark blue); potential vorticity (2 potential vorticity unit (PVU), wtih 1PVU = 10^{-6} (K m^2)/(kg. sec) cyan); potential temperature at 380 K (green); and 100 hPa (black dashed). The proximity of the e90-tropopause to the 2 PVU potential vorticity is in general within the vertical resolution of the model (1–2 km) except in the southern high latitudes where 2 PVU is consistently lower than the e90-tropopause due to the extremely cold air over Antarctica.

In January (Figure 1a), high O_3 mixing ratios in NH extratropics are transported downward but the pathway branches off at 40–50°N in the lower stratosphere going poleward as well as equatorward. The poleward branch eventually converges in the polar region before entering the troposphere, representing the classical descent branch of the BDC into the Arctic, e.g., *Liang et al.* [2009]. The equatorward branch intersects the 250 ppb level at about 40°N and then the 120 ppb and e90-tropopause in the subtropics before entering the troposphere. Poleward transport prevails north of the subtropical jet. However, as the season progresses from winter to summer, the downward transport weakens, and the equatorward transport expands poleward (Figure 1b). By July (Figure 1c), the transport in the LMS is dominantly horizontal and equatorward.

Abalos et al. [2013] analyzed the stratospheric O_3 budget and found: transport due to the advective residual circulation is primarily vertical and that the part due to eddy flux is horizontal and equatorward (see their Figure 7); eddy transport becomes dominant near the 100 hPa level (the lowest level in their analysis); and summertime eddy transport is linked to the Asian anticyclone. In our model, the equatorward, horizontal transport is the main branch intersecting the tropopause (Figures 1a–1c) even during NH winter. For the Southern Hemisphere (SH), a similar progression is seen. Thus, the eddy flux (though not explicitly calculated here) is a major part of the STE O_3 flux.

To evaluate the residual fluxes, we compare the seasonality of the hemispheric residual fluxes across the 100 hPa surface (solid line in Figure 1d) with that of the simulated hemispheric fluxes across the same surface (dashed line in Figure 1d). The simulated O_3 flux peaks in the winter for both NH and SH similar to the findings of *Tie and Hess* [1997] and *Olsen et al.* [2013]. Both residual and simulated fluxes have a similar seasonal cycle in NH, but the total residual flux is about 80% larger. By missing the peak flux in austral winter (JJA), the SH residual flux fails to capture the seasonal cycle. This is due to the large erroneous upward flux inside the SH winter polar vortex (seen in Figure 1f) that cancels the downward flux elsewhere.

In comparison with the flux across the 100 hPa surface, fluxes across the near-tropopause surfaces (TC-e90, TC-120 ppb, and TC-250 ppb in Figure 1e) show smaller seasonal amplitudes with a 2 month lag, which is consistent with Figure 6 in *Hsu et al.* [2005]. While the e90-tropopause surface has the lowest altitude, the associated TC-e90 flux is larger than the TC-120 ppb or TC-250 ppb fluxes for NH spring/early summer and SH summer. The cause is the larger net photochemical production of O_3 in the tropics extending to 30°N between the e90-tropopause and the two O_3 isosurfaces.

The latitudinal distribution of the seasonal average (SON, DJF, MAM, and JJA) downward residual flux across the 100 hPa surface peaks in both hemispheres at 50–70 latitude (Figure 1f); whereas the TC-e90 flux (Figure 1g) peaks at 30°–50° latitude. In the SH, the downward residual flux is confined narrowly near 65°S at the edge the polar vortex and is accompanied by a large upward flux inside the polar vortex, a known erroneous bias of the residual circulation in this region where the zonal mean flow is strong (see discussion in *Miyazaki and Iwasaki* [2008]). The TC-e90 flux peaks during winter and spring in both hemispheres, but the NH has an extended summer peak due to convective enhancement of STE O_3 flux over the continents *Tang et al.* [2011]. Similar patterns apply to the C36 simulations, except that overall climatological means and seasonal variability are both 15–20% smaller.

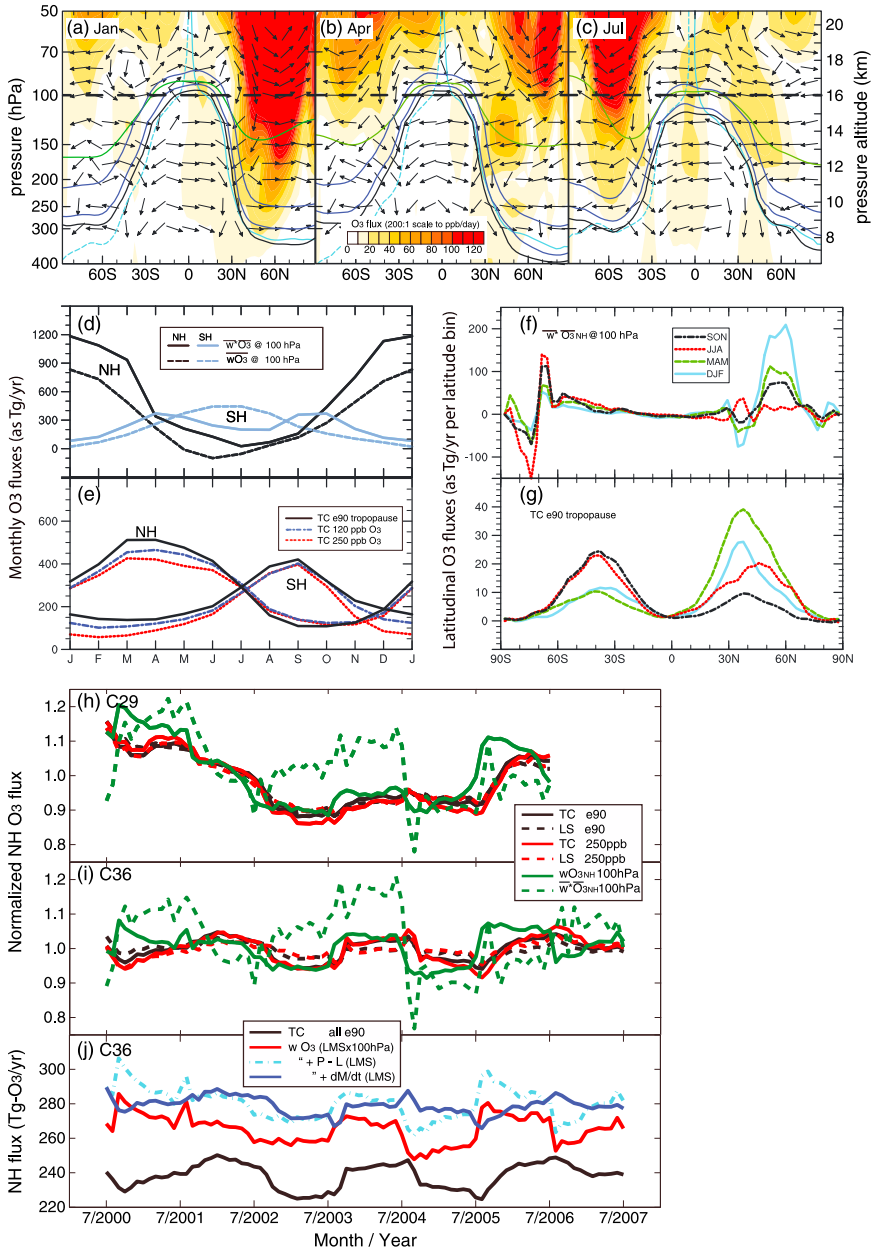

Figure 1. (a–c) Monthly meridional and vertical ozone transport (ppb/d) for the months of January, April, and July averaged over years 2000–2006 with magnitude contoured by colors and directions shown in arrows (see main and supplementary texts for details). (d) Seasonal cycle of hemispherically integrated ozone fluxes across 100 hPa (in Tg/yr). Solid lines are estimates using the monthly mean vertical residual velocity multiplied by the corresponding monthly mean ozone abundances $\overline{w^*}\,\overline{O_3}$. The dashed lines are the exact simulated CTM fluxes $\overline{wO_3}$ across the same level. Both quantities are colored with the NH values in black and the SH in cyan. (e) Same as in Figure 1d but for ozone fluxes across e90-tropopause in black solid line, across 120 ppb-O_3 surface in cyan dash-dotted line and across 250 ppb-O_3 surface in red dashed line. (f) Latitudinal distribution of seasonal ozone fluxes in Tg/yr per latitudinal bin (~ 2.8°) across 100 hPa estimated by $\overline{w^*}\,\overline{O_3}$ with September-October-November (SON) plotted in black, June-July-August (JJA) in red, March-April-May (MAM) in green, and December-January-February (DJF) in cyan. (g) Same as in Figure 1f but for ozone fluxes across e90-tropopause. Color scheme is same as in Figure 1f. Twelve month running mean of normalized NH ozone fluxes across several isosurfaces for (h) C29 and (i) C36. Fluxes across the e90-tropopause are plotted in black; across 250-O_3 surface in red; in solid lines for TC method and dashed lines for LS method. Estimation by the vertical residual velocity is plotted in green dashed line and the exact simulated ozone fluxes across the same surface in green solid line. (j) The NH 12 month running mean ozone flux in Tg/yr across e90-tropopause in black (TC-e90), and in dark blue(LS-e90=$wO_{3\mathrm{LMS@100hPa}} + (P-L)_{\mathrm{LMS}} - \mathrm{d}M/\mathrm{d}t_{\mathrm{LMS}}$). Also, in red is the ozone flux into the LMS ($wO_{3\mathrm{LMS@100hPa}}$), and in cyan, $wO_{3\mathrm{LMS@100hPa}} + (P-L)_{\mathrm{LMS}}$. Inclusion of the LMS tendency term $\mathrm{d}M/\mathrm{d}t_{\mathrm{LMS}}$ in the LMS O_3 budget is crucial for matching the interannual ozone STE variation of TC-e90.

Table 1 summarizes the climatologies of hemispheric O_3 flux for both meteorologies from C29 and C36. They include the mean flux (Flux), the seasonal (S-rms) and interannual (IA-rms) amplitudes, all in the unit of Tg/yr. Also shown is the coefficient obtained from correlating the interannual variation of each flux with TC-e90 flux (IA-r). Results listed downward in rows are from the TC method (TC-e90, TC-120 ppb, and TC-250 ppb), the LS method (LS-e90, LS-120 ppb, and LS-250 ppb), the simulated hemispheric fluxes across 100 hPa ($\overline{wO_{3\,NH}}$), and the residual fluxes ($\overline{w^*}\,\overline{O_3}$) across the 100 hPa surface including the net hemispheric values and the downward only fluxes.

These numbers show how the O_3 flux depends on the choice of "tropopause" isosurface (compare three TC values), and on the consequent LMS domains (compare three LS values). The differences between TC and LS methods reflect fluxes in the tropics where the LMS domains typically do not reach to the equator. For the TC method, the 120 ppb or 250 ppb O_3 isosurfaces reach above the true tropical tropopause (see *Prather et al.* [2011] and *Considine et al.* [2008]) or here the e90-tropopause, and thus, the O_3 production from O_2 photolysis wrongly reduces the net STE into the troposphere, biasing the net STE to lower values. This sometimes does not show up in the LS sequence (C29 NH), but in other cases, the LMS domain has similar biases. The use of an O_3 isosurface is thus not preferred. In the NH, but not SH, seasonal amplitude (S-rms) is larger for e90 than either O_3 surface and truly reflects the seasonality of STE.

3.2. Interannual Variability in the Northern Hemisphere

Interannual variability is calculated from the normalized 12 month running mean of the hemispheric O_3 fluxes and shown for all methods using C29 (Figure 1h) and C36 (Figure 1i). Note that the values plotted for 1 July 2000 are the average of January through December 2000, and the multiyear means and correlations are given in Table 1. Correlation coefficients (listed below under IA-r in Table 1 and the r values discussed below) are calculated relative to the TC-e90 flux, our best estimate. The TC (solid) and LS (dashed) methods are shown for both e90 tropopause (black) and the 250 ppb surface (red). For the most part, these four lines in Figures 1h and 1i are indistinguishable. Fluxes across 100 hPa are shown for both residual (dashed green) and simulated values (solid green). The period from years 2000 to 2007 is relatively quiet climatologically without major volcanic eruptions or El Niño–Southern Oscillation events (based on Southern Oscillation Index from the Climate Prediction Center; www.esrl.noaa.gov/psd/data/climateindices/list/).

For C29 the interannual variability of O_3 fluxes across all isosurfaces near the tropopause, obtained from either TC or LS methods are in near-perfect sync (r = 0.98–1.0), and for C36 they are highly correlated ($r >$ 0.75). For C29 the simulated vertical flux ($\overline{wO_{3\,NH}}$) across 100 hPa is also highly correlated (r = 0.85) and matches even better (r = 0.97) when computed with a 3 month lag for TC-e90. For C36 this vertical flux is weakly correlated (r = 0.41) but greatly improves (r = 0.76) with a 3 month lag as for C29. Thus, in a fast circulation (C29), interannual variability of O_3 fluxes is strongly coupled between the top of the LMS and the tropopause with a 3 month delay and collecting the O_3 fluxes every time step across 100 hPa or similar layer will capture the lagged hemispheric cross-tropopause O_3 flux.

In a more stagnant stratosphere (C36) the coupling is not as strong and is mostly lost in the irregular buffering capacity of the lowermost stratospheric air mass. To understand this, one can look at the components of the O_3 budget in the LS method (see Figure 1j). Note that the 100 hPa flux for the LS domain is calculated from the pole to the intersect with the e90 surface near the tropics (denoted with the subscript LMS in Figure 1j), whereas the simulated hemispheric flux (green solid line in Figure 1i) is calculated from the pole to the equator. The downward flux entering the LMS across the 100 hPa surface correlates weakly with the TC-e90 flux (r = 0.18). Adding the photochemical term reduces the correlation (to r = 0.10). However, further adding the lowermost stratospheric mass tendency increases the correlation drastically to 0.82. Thus, small interannual variations in the lowermost stratospheric O_3 mass (±25 Tg/yr) control the long-term variability of O_3 STE for the stagnant circulation of C36.

The residual O_3 flux, $\overline{w^*}\,\overline{O_3}$, across 100 hPa (green dashed line) appears jagged in Figures 1h and 1i, despite being a 12 month average, with a low correlation to TC-e90 for both C29 (r = 0.36) and C36 (r = 0.06). The correlation is similar if we only count the downward O_3 flux north of 40° latitude but is much poorer if the downward only flux of air ($w^* >$0) is used as a proxy for the STE flux. These correlations also do not improve if one allows for a time lag.

It is surprising that the two different versions of the IFS forecast system do not show more correlation for most of the calculated fluxes given that both are forecasting the same assimilated fields. The cross

AGU Geophysical Research Letters

10.1002/2014GL061994

Table 1. Net Stratosphere-Troposphere Exchange (STE) of O_3 by Hemisphere (Tg/yr) Calculated Using a Variety of Diagnostic Methods Within a Chemistry-Transport Model Simulation[a]

	NH Cycle 29				NH Cycle 36				SH Cycle29				SH Cycle 36			
Methodology	Flux	S-	IA-	IA-r	Flux	S-	IA-	IA-r	Flux	S-	IA-	IA-r	Flux	S-	IA-	IA-r
TC e90-tropopause	301	153	22	1.00	239	115	7	1.00	233	95	11	1.0	198	86	9	1.00
TC 120 ppb O_3 surface	289	129	22	1.00	219	92	7	0.98	205	100	13	0.98	162	88	10	0.98
TC 250 ppb O_3 surface	270	117	23	1.00	200	78	8	0.97	176	116	16	0.95	132	107	11	0.95
LS e90 tropopause	313	146	22	0.98	279	108	5	0.82	235	94	11	0.99	220	84	8	0.98
LS 120 ppb O_3 surface	314	122	19	0.91	243	88	5	0.33	220	95	13	0.98	166	79	11	0.96
LS 250 ppb O_3 surface	313	118	21	0.98	254	82	5	0.76	218	112	13	0.97	171	94	11	0.93
$\overline{wO_3}$ 100 hPa surface	311	316	29	0.85	238	246	11	0.41	224	147	12	0.36	166	118	7	0.35
$\overline{w^*}\,\overline{O_3}$ 100 hPa surface	537	431	51	0.36	446	383	42	0.06	237	98	51	−0.12	147	78	31	−0.13
$\overline{w^*}\,\overline{O_3} > 0$@ 100 hPa surface	1244	849	64	0.32	1069	748	62	0.12	1098	391	100	−0.13	917	357	118	−0.27

[a]Results are based on two multiyear meteorologies from cycle 29r1 and cycle 36r1 of the ECMWF IFS forecasts running in the UCI CTM. Mean fluxes (Flux) are integrated for each hemisphere, averaged over years 2000–2006 for C29 and 2000–2007 for C36, in units of Tg-O_3 per year. The mean seasonal variations (S-RMS) are calculated from the 12 monthly means. The interannual variations (IA-RMS) are calculated from the annual fluxes evaluated at each month using a 12 month running mean. The interannual correlation coefficients (IA-r) are calculated relative to our best value, the TC e90-tropopause flux. Tropospheric column (TC) methods calculate the O_3 flux across a surface at every time step in the model and resolve them geographically and temporally at the model resolution. We have chosen three surfaces (e90-tropopause and O_3 surfaces at 120 ppb and 250 ppb) at which to evaluate this flux. Lowermost stratosphere (LS) methods are based on the changes in the O_3 content in the LMS region between 100 hPa (upper surface) and the lower surface defined by e90 or O_3 abundances. The simulated flux across the 100 hPa surface ($\overline{wO_{3\,\mathrm{NH}}}$) is monthly average accumulated every model time step. The residual O_3 flux across 100 hPa is calculated based on the monthly mean vertical residual velocity ($\overline{w^*}$) from the transformed Eulerian mean equations and the monthly zonal mean O_3 abundance ($\overline{O_3}$). Also, shown is $\overline{w^*}\,\overline{O_3} > 0$ (define downward being positive), the downwelling ozone flux integrated poleward of 40° across 100 hPa surface.

correlation between the corresponding C29 STE flux and C36 STE flux ranges from 0.4 to 0.5 for three TC pairs and the LS-e90 pair, and is nearly zero for the other two LS pairs. In contrast, the residual O_3 fluxes controlled by the large-scale BDC between these two cycles appear well correlated at the value of 0.9. Hence transport within the LMS, below 100 hPa, is very sensitive to the forecast model here.

4. Discussion and Conclusion

This work presents a self-consistent calculation of the net O_3 STE using a range of currently applied methods. We implement the same calculation in two simulations driven by two multiyear sets of ECMWF-IFS data that have distinctly different stratospheres in terms of the strength of the Brewer-Dobson circulation, lateral mixing, and consequently age-of-air and N_2O lifetime. In each simulation, our geographically resolved O_3 STE derived from the tropospheric column budget agree well with one another as long as the STE boundary is close to the tropopause (e.g., e90-tropopause tracer, O_3 levels of 120 or 250 ppb). They also agree with the hemispheric fluxes inferred from the O_3 budget of the LMS. The simulated NH flux across the 100 hPa surface leads the NH O_3 STE flux in time by 2–3 months.

Using the stratospheric overturning circulation as quantified by the transformed Eulerian mean vertical velocity $\overline{w^*}$ to calculate, or even act as a scalable proxy for, the STE O_3 flux, however, yields serious errors. For instance, in cycle 29 simulation, the mean NH residual O_3 fluxes, $\overline{w^*}\,\overline{O_3}$, are about twice (537 Tg/yr) as large compared to STE fluxes and the simulated fluxes across the same level ($\sim$ 300 Tg/yr $\pm$ 5%). Moreover, they do not capture the interannual climate variability (and possibly long-term change) as they do not correlate well with all other fluxes, which are largely in sync with each other. Use of just the downward hemispheric residual air mass flux, $\overline{w^*} > 0$, is likewise erroneous.

A stronger Brewer-Dobson circulation indeed means a larger downward O_3 flux. However, the increase does not scale linearly across all time scales because the eddy transport and the irregular buffering through the change in the lowermost stratospheric volume mass are also important factors for determining where and when STE of O_3 takes place. With a stronger BDC in the simulation driven by ECMWF-IFS cycle 29r1 compared to cycle 36r1, the NH mean and seasonal variability of O_3 STE are about 20–40% larger, but the interannual variability is larger by a factor of 3–4. Most importantly between these two simulations, the temporal variation for the residual fluxes driven the BDC remains similar to each other but very different for all other O_3 fluxes. Such differences are also likely to occur across different CCM models, if we apply accurate flux diagnostics methods. Thus, the two simulations, based on ECMWF IFS data, provide a good analog for different chemistry-climate models and climate change simulations. As similarly pointed out in *Olsen et al.* [2013], one cannot simply quantify the multiyear downward transport by the BDC using the residual advective velocity and scale it to represent the corresponding O_3 STE.

We recommend that STE O_3 fluxes be directly calculated in numerical models using the tropospheric column method, because it allows the spatial distribution of STE to be accurately diagnosed. Thus, the influence of changing STE on regional air quality can also be accessed. Use of the lowermost stratospheric O_3 budget is limited to diagnose broad hemispheric quantities, perhaps the radiative forcing. It is more readily applied to observed measurements if the monthly variation of the LMS can also be accurately tracked. At a minimum, integrating the vertical fluxes across 100 hPa every time step with a lead time of 3 months to cross-tropopause fluxes is a more accurate proxy for the interannaul variability of STE than computing the monthly mean vertical residual velocity at the same level. The full CCM simulations will implicitly include the effects of changing STE O_3 flux on tropospheric O_3, but there are many factors influencing tropospheric O_3 (e.g., overhead column O_3), and thus, there is a need to accurately diagnose this key component of the tropospheric O_3 budget.

Acknowledgments
This research was supported by the NASA Modeling, Analysis, and Prediction Program (NNX13AL12G), the Office of Science (BER) of the U.S. Department of Energy (DE-SC0007021), and the Kavli Chair in Earth System Science. The diagnostics of O_3 flux presented in this study are publicly available at the anonymous ftp site halo.ess.uci.edu under /public/juno/2014GL061994/.

The Editor thanks two anonymous reviewers for their assistance in evaluating this paper.

References

Abalos, M., F. Ploeger, P. Konopka, W. J. Randel, and E. Serrano (2013), Ozone seasonality above the tropical tropopause: Reconciling the Eulerian and Lagrangian perspectives of transport processes, *Atmos. Chem. Phys.*, *13*(21), 10,787–10,794.

Andrews, D., J. Holton, and C. Leovy (1987), *Middle Atmosphere Dynamics*, 481 pp., Acad. Press Inc., Orlando, Fla.

Appenzeller, C., J. R. Holton, and K. H. Rosenlof (1996), Seasonal variation of mass transport across the tropopause, *J. Geophys. Res.*, *101*, 15,071–15,078.

Butchart, N., et al. (2010), Chemistry-climate model simulations of twenty-first century stratospheric climate and circulation changes, *J. Clim.*, *23*, 5349–5374, doi:10.1175/2010JCLI3404.1.

Considine, D. B., J. A. Logan, and M. A. Olsen (2008), Evaluation of near-tropopause ozone distributions in the Global Modeling Initiative combined stratosphere/troposphere model with ozonesonde data, *Atmos. Chem. Phys.*, *8*, 2365–2385.

Eyring, V., et al. (2013), Long-term ozone changes and associated climate impacts in CMIP5 simulations, *J. Geophys. Res. Atmos.*, *118*, 5029–5060, doi:10.1002/jgrd.50316.
Fiore, A. M., et al. (2012), Global air quality and climate, *Chem. Soc. Rev.*, *41*, 6663–6683, doi:10.1039/C2CS35095E.
Gettelman, A., and A. H. Sobel (2000), Direct diagnoses of stratosphere-troposphere exchange, *J. Atmos. Sci.*, *57*(1), 3–16.
Gettelman, A., J. R. Holton, and K. H. Rosenlof (1997), Mass fluxes of O3, CH4, N2O and CF2Cl2 in the lower stratosphere calculated from observational data, *J. Geophys. Res.*, *102*(D15), 19,149–19,159.
Hegglin, M. I., and T. G. Shepherd (2009), Large climate-induced changes in ultraviolet index and stratosphere-to-troposphere ozone flux, *Nat. Geosci.*, *2*, 687–691.
Holton, J. R. (1990), On the global exchange of mass between the stratosphere and troposphere, *J. Atmos. Sci.*, *47*, 392–395, doi:10.1175/1520-0469.
Holton, J. R., P. H. Haynes, M. E. McIntyre, A. R. Douglass, R. B. Rood, and L. Pfister (1995), Stratosphere-troposphere exchange, *Rev. Geophys.*, *33*, 403–439.
Hsu, J., and M. J. Prather (2009), Stratospheric variability and tropospheric ozone, *J. Geophys. Res.*, *114*, D06102, doi:10.1029/2008JD010942.
Hsu, J., and M. J. Prather (2010), Global long-lived chemical modes excited in a 3-D chemistry transport model: Stratospheric N2O, NOy, O3 and CH4 chemistry, *Geophys. Res. Lett.*, *37*, L07805, doi:10.1029/2009GL042243.
Hsu, J., M. J. Prather, and O. Wild (2005), Diagnosing the stratosphere-to-troposphere flux of ozone in a chemistry transport model, *J. Geophys. Res.*, *110*, D19305, doi:10.1029/2005JD006045.
Liang, Q., A. R. Douglass, B. N. Duncan, R. S. Stolarski, and J. C. Witte (2009), The governing processes and timescales of stratosphere-to-troposphere transport and its contribution to ozone in the Arctic troposphere, *Atmos. Chem. Phys.*, *9*, 3011–3025, doi:10.5194/acp-9-3011-2009.
Logan, J. A., M. J. Prather, S. C. Wofsy, and M. B. McElroy (1981), Tropospheric chemistry: A global perspective, *J. Geophys. Res.*, *86*(C8), 7210–7254.
McLinden, C. A., S. Olsen, B. Hannegan, O. Wild, M. J. Prather, and J. Sunder (2000), Stratospheric ozone in 3-D models: A simple chemistry and the cross-tropopause flux, *J. Geophys. Res.*, *105*, 14,653–14,665.
Miyazaki, K., and T. Iwasaki (2008), On the analysis of mean downward velocities around the Antarctic polar vortex, *J. Atmos. Sci.*, *65*, 3989–4003, doi:10.1175/2008JAS2749.1.
Myhre, G., et al. (2013), Anthropogenic and natural radiative forcing, in *Climate Change 2013: The Physical Science Basis. Contribution of Working Group I to the Fifth Assessment Report of the Intergovernmental Panel on Climate Change*, edited by T. F. Stocker et al., Cambridge Univ. Press, Cambridge, U. K., and New York.
Olsen, M. A., M. R. Schoeberl, and A. R. Douglass (2004), Stratosphere-troposphere exchange of mass and ozone, *J. Geophys. Res.*, *109*, D24114, doi:10.1029/2004JD005186.
Olsen, M. A., A. R. Douglass, and T. B. Kaplan (2013), Variability of extratropical ozone stratosphere-troposphere exchange using Microwave Limb Sounder observations, *J. Geophys. Res. Atmos.*, *118*, 1090–1099, doi:10.1029/2012JD018465.
Prather, M. J. (1986), Numerical advection by conservation of 2nd-order moments, *J. Geophys. Res.*, *91*(D6), 6671–6681.
Prather, M. J., X. Zhu, S. E. Strahan, S. D. Steenrod, and J. M. Rodriguez (2008), Quantifying errors in trace species transport modeling, *Proc. Nat. Acad. Sci. U.S.A.*, *105*(50), 19,617–19,621.
Prather, M. J., X. Zhu, Q. Tang, J. Hsu, and J. L. Neu (2011), An atmospheric chemist in search of the tropopause, *J. Geophys. Res.*, *116*, D04306, doi:10.1029/2010JD014939.
Stevenson, D. S., R. M. Doherty, M. G. Sanderson, W. J. Collins, C. E. Johnson, and R. G. Derwent (2004), Radiative forcing from aircraft NOx emissions: Mechanisms and seasonal dependence, *J. Geophys. Res.*, *109*, D17307, doi:10.1029/2004JD004759.
Stevenson, D. S., et al. (2006), Multimodel ensemble simulations of present-day and near-future tropospheric ozone, *J. Geophys. Res.*, *111*, D08301, doi:10.1029/2005JD006338.
Strahan, S. E., et al. (2011), Using transport diagnostics to understand chemistry climate model ozone simulations, *J. Geophys. Res.*, *116*, D17302, doi:10.1029/2010JD015360.
Tang, Q., M. J. Prather, and J. Hsu (2011), Stratosphere-troposphere exchange ozone flux related to deep convection, *Geophys. Res. Lett.*, *38*, L03806, doi:10.1029/2010GL046039.
Thompson, A. M. (1992), The oxidizing capacity of the Earth's atmosphere: Probable past and future change, *Science*, *256*(5060), 1157–1165, doi:10.1126/science.256.5060.1157.
Tie, X. X., and P. Hess (1997), Ozone mass exchange between the stratosphere and troposphere for background and volcanic sulfate aerosol conditions, *J. Geophys. Res.*, *102*(D21), 25,487–25,500.
Waugh, D. W., and T. M. Hall (2002), Age of stratospheric air: Theory, observations, and models, *Rev. Geophys.*, *40*(4), 1010, doi:10.1029/2000RG000101.
Wei, M. Y. (1987), A new formulation of the exchange of mass and trace constituents between the stratosphere and troposphere, *J. Atmos. Sci.*, *44*(20), 3079–3086.
Young, P. J., et al. (2013), Pre-industrial to end 21st century projections of tropospheric ozone from the Atmospheric Chemistry and Climate Model Intercomparison Project (ACCMIP), *Atmos. Chem. Phys.*, *13*, 2063–2090, doi:10.5194/acp-13-2063-2013.